ELSEVIER

Polymer Vol. 37 No. 15, pp. 3265–3272, 1996

0032-3861/96/$15.00 + 0.00

Effects of compaction pressure on cohesive strength and chain mobility of low-temperature compacted nascent UHMWPE

P. Gao*, Man Ken Cheung and T. Y. Leung
Department of Chemical Engineering, The Hong Kong University of Science and Technology, Clear Water Bay, Kowloon, Hong Kong
(Received 16 August 1995; revised 20 November 1995)

The effects of compaction pressure on the deformability of the compacted nascent ultra high molecular weight polyethylene (UHMWPE) precursors were investigated. High-temperature solid-state nuclear magnetic resonance studies show that an optimum compaction pressure exists for the compacted precursors to retain maximum chain mobility in the amorphous phase. The optimum compaction condition also produces the maximum mechanical toughness, as determined by universal testing machine and maximum crystal sizes as implied by differential scanning calorimetry. An attempt was also made to elucidate the mechanisms for particle interfacial diffusion between the compacted UHMWPE powders. A sufficiently high compaction pressure is needed to produce a large contact surface area for intimate molecular contact at particle boundaries enabling interfacial diffusion. The diffused chains can either crystallize to give larger crystal sizes or form entanglements with their new neighbouring chains. These recrystallization and re-entanglement processes which occur at the particle boundaries will give enhanced particle interfacial cohesive strength, resulting in high mechanical toughness for the compacted material. However, when the compaction pressure reaches a critical value at which the product of the contact surface area and the free volume available for chain movement reaches maximum, the interfacial diffusion will start to decrease. Further increase in compaction pressures might result in a decrease in particle cohesive strength. Cohesive precursors with high chain mobility are ideal for further tensile drawing into high stiffness films or fibres.

(Keywords: nascent UHMWPE; solid state n.m.r.; d.s.c. analysis)

INTRODUCTION

In the last fifteen years, a number of related process routes have been developed to produce high stiffness and high strength fibres from ultra high molecular weight polyethylene (UHMWPE) materials following the invention of gel spinning technology[1]. The ultimate tensile properties of the gel spun fibre depend on the initial solvent loading. It was proposed that the presence of solvent causes a reduction in physical entanglement density, and thus results in higher ductility of the gel material. Variants of gel spinning processes include swell drawing[2–4] and die free spinning[5]. The apparent disadvantage of such processes is the use of organic solvents, which are difficult to recycle and to remove.

Alternative routes include ram extrusion or drawing of low-entanglement reactor powders[6–9]. Such processes include the compaction or ram extrusion of the low entanglement reactor powders at a temperature close to, but lower than, the melting point of the reactor powder followed by tensile drawing at an elevated temperature. A high stiffness of 116 GPa was obtained by Smith *et al.*[7] by hot drawing of compacted nascent reactor powders. Wang and Porter[9] have shown that a fibre with a Young's modulus of 68 GPa and a tensile strength of 1.3 GPa was produced by roll-stretching a commercial UHMWPE Hifax reactor powder to a draw ratio of 73. However, the maximum drawability of the reactor powder might still not have been achieved, due to two major factors. Firstly, premature failure at the particle interfaces could have occurred during the drawing of the compacted precursors if the interfacial cohesive strength between the particles was low. Secondly, the compaction might not have been able to retain the maximum ductility of the Nascent powders. Some preliminary studies have been carried out on the effect of compaction temperature on the drawability of compacted powders[7]. However, no systematic studies have been reported so far on the effect of compaction conditions on particle interfacial cohesion and chain mobility after compaction.

The primary objective of this paper is to describe the experimental observations that we have made on solid-state compacted commercially available low entanglement UHMWPE reactor powders and to discuss these results in terms of possible interfacial cohesion mechanisms during the compaction process.

EXPERIMENTAL

Materials and sample preparation

The polymer used in this study was UHMWPE Hifax 1900, kindly supplied by Montell. The weight-average

* To whom correspondence should be addressed

molecular weight for Hifax 1900 is about 6×10^6, and the as-received reactor powder has an average particle size of about 200 μm. The differential scanning calorimetry (d.s.c.) melting transition temperature for this material is 143.5°C. A normal high-entanglement UHMWPE UH210 manufactured by DSM is also used for comparison.

The reactor powders as received were compacted using a capillary rheometer (Goffert Rheograph 2003) at 127°C under different compaction pressures for a duration of 30 min. The temperature chosen here corresponds to the optimum temperature reported by Smith *et al.*[7]. The compaction time of 30 min was considered to be sufficient for a uniform temperature profile to develop within the compacted powders. The barrel of the rheometer has a bore diameter of 12 mm and a length of 200 mm. The end of the barrel was blocked off with a solid cylinder die block for compaction. For each sample preparation, 15 g of reactor powder was used and was charged slowly with intermittent compaction to minimize air trapping. After the compacted rod was removed from the barrel, it was allowed to cool for at least 24 h prior to any testing.

Differential scanning calorimetry measurement

Melting endotherms were recorded using a DuPont TA 2910 differential scanning calorimeter. A sample weight of approximately 5 mg and a standard heating rate of 10°C min^{-1} were chosen. Indium was used for temperature calibration (melting transition temperature, $T_m = 156.6$°C). For compacted powders, all samples were taken from the centre of the compacted rods to avoid any effects due to temperature gradients which might have been present during compaction.

Uncompacted powder samples. *Figure 1* shows the thermographs for the as-received powder samples of UHMWPE Hifax 1900 and UH210. The Hifax 1900 powder shows both a higher T_m, with $T_m = 143.5$°C, and a larger heat of fusion, $\Delta H = 204.0\ J\ g^{-1}$, whereas the UH210 reactor powder has a first heating $T_m = 139.6$°C and $\Delta H = 176.9\ J\ g^{-1}$.

There is a small difference of 3.9°C, or 2.7%, between the two first heating T_ms. However, the heat of fusion of the Hifax 1900 reactor powder is $27.1\ J\ g^{-1}$, or 15.3%, greater than that of the UH210 reactor powder. The larger heat of fusion value indicated a greater crystallinity present in the Hifax 1900 material, 70%, against 60% for the UH210 sample. The crystallinity was calculated by assuming $\Delta H = 293\ J\ g^{-1}$ for the 100% crystallinity of polyethylene[10]. The higher T_m for Hifax 1900 is thought to be due to the fast annealing effect which occurs during the d.s.c. heating process[11]. The lack of entanglement constraints in the amorphous phase for Hifax 1900 reactor powders give the chains very high mobility, which then reorganize into larger crystals rapidly upon the d.s.c. heating process.

On cooling and reheating, however, both show similar thermal properties. The reheating produces T_ms of 135.9°C and 132.8°C, for Hifax 1900 and UH210 reactor powders, respectively. ΔH on reheating is $137.6\ J\ g^{-1}$ for the former and $135.3\ J\ g^{-1}$ for the latter. These figures imply that after the first heating the crystallinity in both powders decreases. The crystallinities are 47% for Hifax 1900 and 46% for UH210 reactor powder with a greater reduction in crystallinity for the Hifax 1900 reactor powder. These observations are consistent with the results reported by Lemstra and Kirschbaun[12]. They reported that the low entanglement gel crystallized material showed a complete loss of ductility upon heating above its melt transition temperature, and the molten/recrystallized sample was indistinguishable from a normal high entanglement UHMWPE.

Compacted samples. The UH210 cannot be compacted into a coherent powder, as shown in the scanning electron microscope (SEM) photograph (*Figure 7*), and there was little observed change in its melting endotherms at different compaction pressures. For Hifax 1900, the compaction pressure appears to show a strong influence on T_m, as shown in *Figure 2*. There are two regions of influence. The first covers the compaction pressure range from 0 to 30 MPa and the second from 30 to 100 MPa. There is a possible third region, above 100 MPa, where T_m might prove to be constant with increasing compaction pressure. However, this is speculative and would need to be confirmed by further

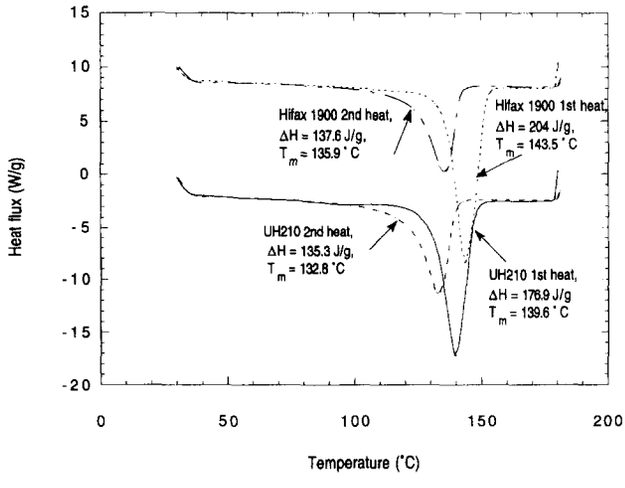

Figure 1 D.s.c. thermographs of UHMWPE Hifax 1900 and UH210 reactor powders with a heating rate of 10°C min^{-1}

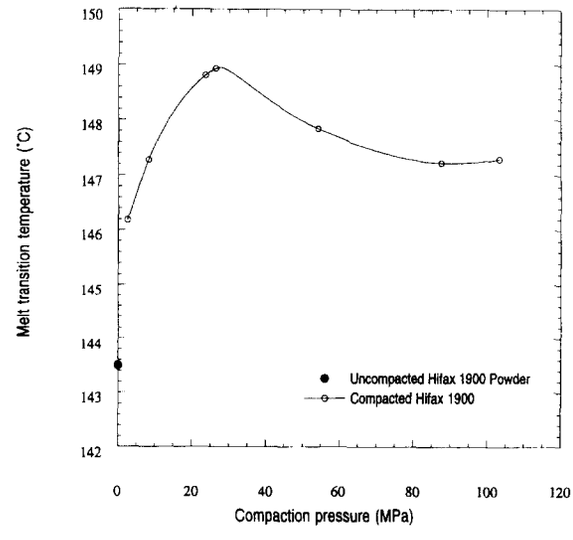

Figure 2 T_m *versus* compaction pressure for UHMWPE Hifax 1900 samples compacted at 127°C for 30 min

experiments. In the compaction pressure range from 0 to 30 MPa, T_m showed an increase of approximately 6°C. In the second region, a small drop of 2°C is observed.

The crystallinity, however, does not appear to be affected by compaction pressure as shown in *Figure 3*. The d.s.c. crystallinity remains at approximately 80% over the whole compaction pressure range studied. The only exception is for the as-received reactor powder which has a low crystallinity of 72%. We attribute the difference to the annealing time. For the compacted samples, annealing time at 127°C was 30 min, whereas for the reactor powders the only annealing time was during the d.s.c. heating process, and the time duration for annealing was less than 2 min.

The fact that the crystallinity does not vary with compaction pressure implies that the change in T_m was due to the chain mobility change in the amorphous phase. In the compaction pressure range between 0 and 30 MPa, the increase in compaction pressure provides an increase in particle surface contact area. Therefore, the mobile chains in the amorphous phase are able to diffuse across particle boundaries to form entanglements. At the higher compaction pressures, the reduction in free volume probably caused a greater rigidity of the particles. This might result in a slow down of the diffusion of the chains in the amorphous region and the recrystallization process. This is further demonstrated in the bulk density data, determined by simply measuring the dimensions and weighing the compacted rod samples, as shown in *Figure 4*. The density increases from 855 to 955 kg m^{-3} in the first region for compaction pressure ranging from 2.7 to 30 MPa and decreases slightly to 948 kg m^{-3} at 100 MPa in the second region. When the bulk density reaches its maximum value, any further increase in compaction pressure is expected to reduce the free volume available for chain diffusion.

Morphological analysis

An SEM (type JEOL 6300) was used to examine the morphology of the as-received reactor powders and the fractured compacted powder samples. Samples were

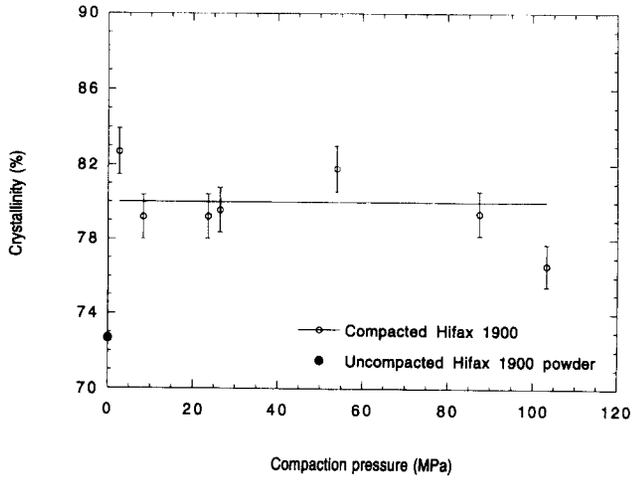

Figure 3 D.s.c. crystallinity *versus* compaction pressure for UHMWPE Hifax 1900 samples compacted at 127°C for 30 min. The effects of compaction pressure on crystallinity is negligible. Therefore, the variation of T_m with compaction pressure shown in *Figure 2* is due to the variation of chain mobility in the amorphous phase, which leads to the variation in degree of reorganization into crystals

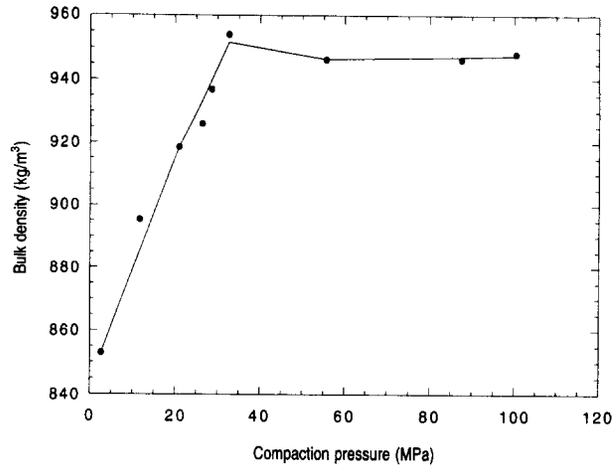

Figure 4 Variation of bulk density of UHMWPE Hifax 1900 samples prepared at 127°C for 30 min. This suggests that denser particle aggregates were obtained with increasing compaction pressure until about 30 MPa, while further increase in compaction pressure reduces the free volume available chain diffusion across particle boundaries to reorganize into crystals

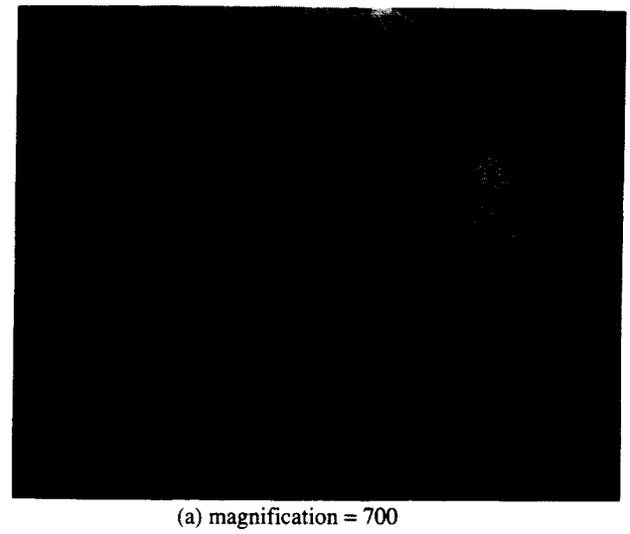

(a) magnification = 700

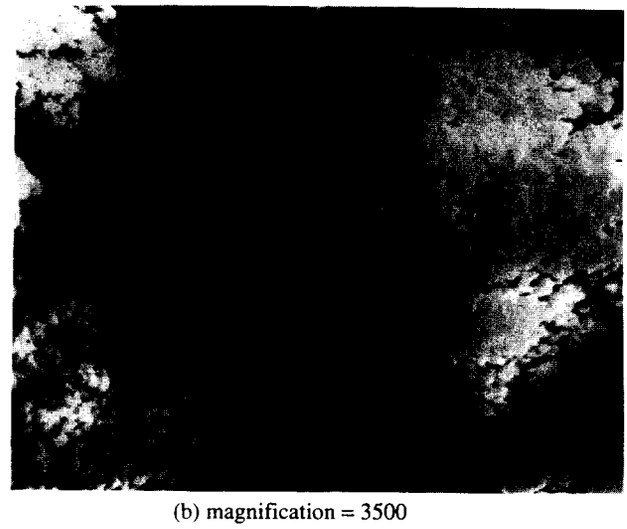

(b) magnification = 3500

Figure 5 SEM photographs of an as-received UHMWPE Hifax 1900 reactor powder at two different magnifications. (a) Magnification = 700 and (b) magnification = 3500

coated with a thin layer of gold (ca. 10 nm) using a sputter coater to avoid charging before observation under SEM. The photomicrographs were taken at 5 kV and 150 mA to minimize surface heating effect.

Uncompacted powder samples. Figures 5a–5b and *6a–6b* show the surface morphology of the uncompacted UHMWPE Hifax 1900 and UH210 reactor powder, respectively, at two different magnifications. For both powders, it can be seen that the major powder particles are made up of smaller minor powder particles which have formed aggregates. The minor powder particles, with diameter of the order 10 μm, are further represented by an aggregate of numerous submicron fine particles.

These SEM photographs show that there is a greater degree of microscopic segregation between the minor particles in the Hifax 1900 reactor powder than in the UH210 reactor powder. Indeed, the UH210 reactor powder shows a great deal of interconnectivity between the minor particles, with many fibrillar bridges. The near absence of connecting fibrillar bridges in Hifax 1900 reactor powder indicates little or no partial melting during synthesis.

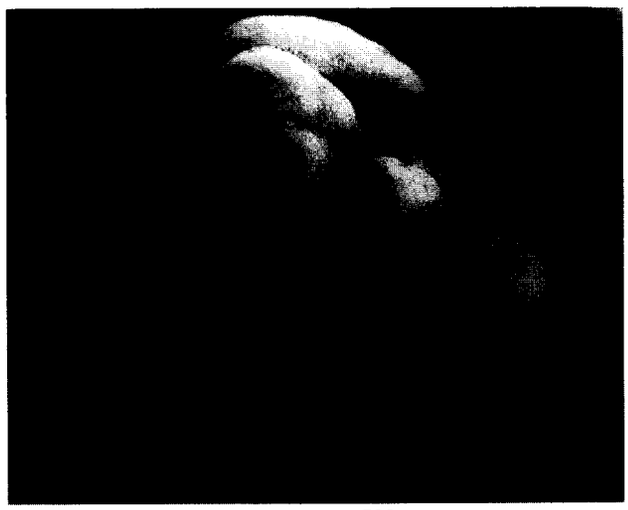

(a) magnification = 700

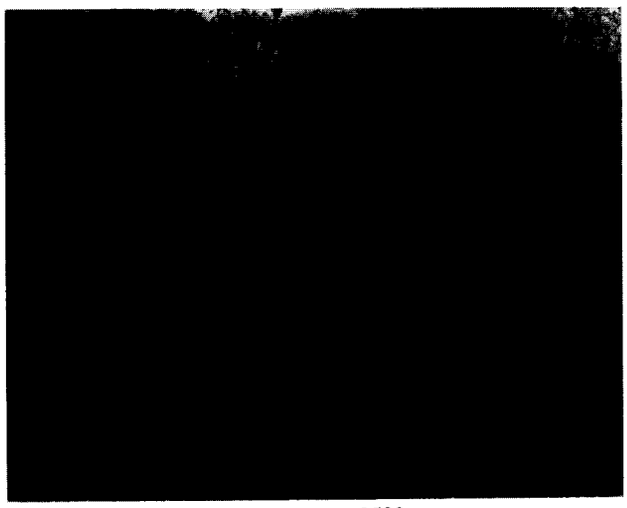

(b) magnification = 3500

Figure 6 SEM photographs of an as-received UHMWPE UH210 reactor powder at two different magnifications. (a) Magnification = 700 and (b) magnification = 3500

Compacted samples. Figures 7 and *8d* are SEM photographs of compacted UH210 (compaction pressure was 90.87 MPa) and Hifax 1900 (compaction pressure was 110.6 MPa), respectively. It is clear that under compaction both the major and minor particles in the Hifax 1900 powder undergo intimate molecular contact at the particle boundaries. UH210, however, does not undergo the same degree of cohesion, especially between the major powder particles.

The effect of compaction pressure on morphology of compacted Hifax 1900 samples is shown in *Figures 8a–8d*. The photos were taken on cryogenically fractured surfaces by immersing samples in liquid nitrogen. On the application of a low compaction pressure of 6.0 MPa, both the major and minor particles started to flow into each other (*Figure 8a*). This was the initiation of interfacial cohesion. The enhancement of this interfacial cohesion is observed with increasing compaction pressure. This enhancement can be seen for samples processed under compaction pressures up to approximately 20 MPa (*Figure 8b*). Further, there is also evidence of cohesive failure during cryogenic fracture on the surface. This is shown by the extended fibre structure as indicated by the arrow bars. After this, the differences in morphology are difficult to resolve. However, a significant change in morphology was observed for samples compacted at the compaction pressure of 110.9 MPa (*Figure 8d*). While all the other compacted samples (*Figures 8a–8c*) still retain the memory of their initial powder morphology represented by the appearance of aggregates of submicron fine particles within each minor particle, the sample compacted at 110.9 MPa appears to have lost the memory of these fine particles.

Mechanical toughness measurements

In order to evaluate the cohesive strength of the compacted powders, mechanical toughness of the compacted rod samples is measured. We have chosen to use the universal testing machine (UTM) to measure the volumetric energy to fracture at a low cross-head displacement speed due to the brittle nature of the compacted specimens. Young's modulus was also measured and the measurements were performed on a

Figure 7 SEM photograph of an UHMWPE UH210 sample compacted at 90.9 MPa and 127°C for 30 min. The magnification of the photograph is 1200

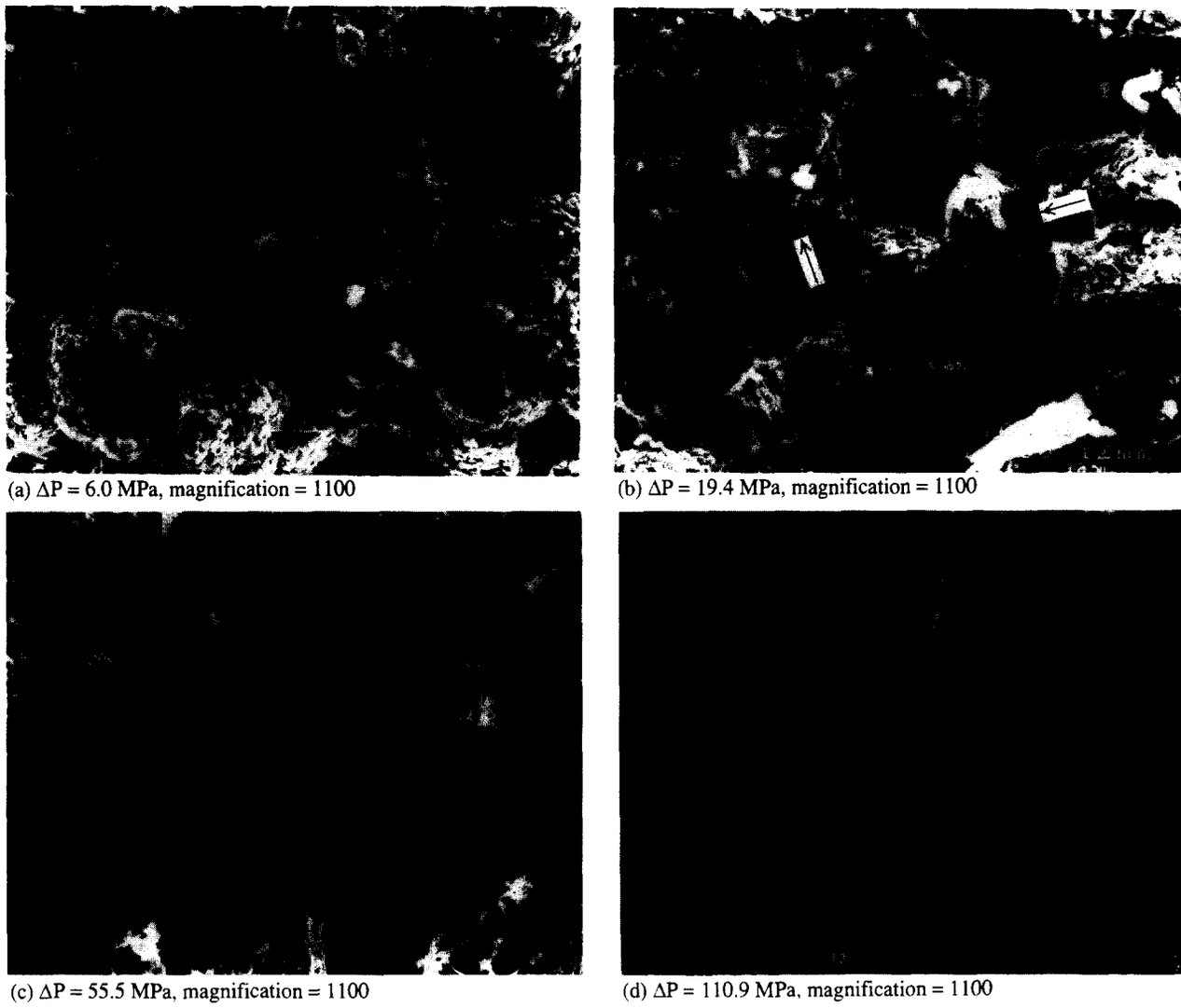

(a) ΔP = 6.0 MPa, magnification = 1100

(b) ΔP = 19.4 MPa, magnification = 1100

(c) ΔP = 55.5 MPa, magnification = 1100

(d) ΔP = 110.9 MPa, magnification = 1100

Figure 8 SEM photographs of UHMWPE Hifax 1900 samples compacted at 127°C for 30 min. The magnification of the photographs is 1100. The arrows indicate the cohesive failure that occurred during fracture

Sintech UTM with a maximum capacity of 50 kN. Since the fabricated rods were too brittle to be directly clamped to the UTM, specially designed grips were added to the ends of each rod sample[13]. For each measurement, the fabricated rods were machined into dumb-bell shaped samples and loaded between the grips. Strain gauges with a resistance of 120 Ω and a surface area of 10 mm × 5 mm were then cemented onto the reduced area, with a diameter of 8 mm and a length of 20 mm, in order to determine the strain during testing. The extensometer was not used here because the material was too brittle. Fracture should occur in the reduced-area region and not in the gripping region, otherwise the weakening effect in the gripping region might affect the result validity. The measurements were performed at a cross-head speed of 0.1 in min^{-1} at the ambient temperature.

Figure 9 shows a typical stress–strain curve for Hifax 1900 specimen compacted at a pressure of 32.6 MPa at 127°C. The material apparently shows a brittle failure at fracture and has a maximum elongation at break of about 0.14%. No necking was observed for all the samples tested. Therefore, the energy absorbed prior to fracture per unit deformation volume can be obtained by a simple integration of the stress–strain curve[14]. Results of energy to fracture *versus* compaction pressure obtained in this way are shown in *Figure 10*. The reported results were the average values over two repeated tests performed on two different specimens which were within the measurement error range ±10%.

The results can again be divided into two regions. The first region is for the pressure ranging from 12 to 32 MPa and the second is from 32 to 100 MPa. In the first part, the energy absorbed before fracture increases from 2.5 kJ m^{-3} to 4.8 kJ m^{-3}, while, in the second region, the energy to fracture decreases to 2.8 kJ m^{-3}. It should be noted that the data scattering appears to be significant. However, the maximum change in energy to fracture for samples compacted under different pressures is greater than 100%, i.e. far greater than the maximum errors, and both data sets show a similar trend. Further, at least four samples were measured at compaction pressures close to 30 MPa and the values obtained are all much higher than samples compacted at either very high or very low compaction pressures. It can therefore be concluded that the trend ascertained is reliable.

The ultimate tensile stress–strain represents the total energy absorbed per deformation volume before fracture.

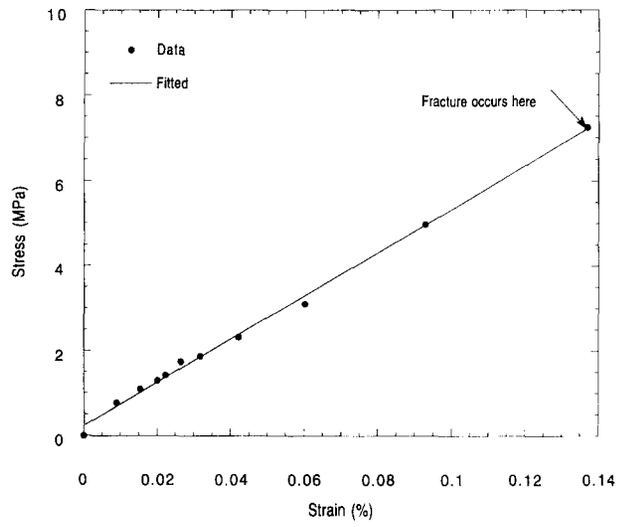

Figure 9 A typical stress–strain curve for a compacted UHMWPE Hifax 1900 specimen measured at the ambient temperature. The compaction conditions were set at 32.7 MPa, 127°C and 30 min. The cross-head displacement speed was 2.5 mm min^{-1}

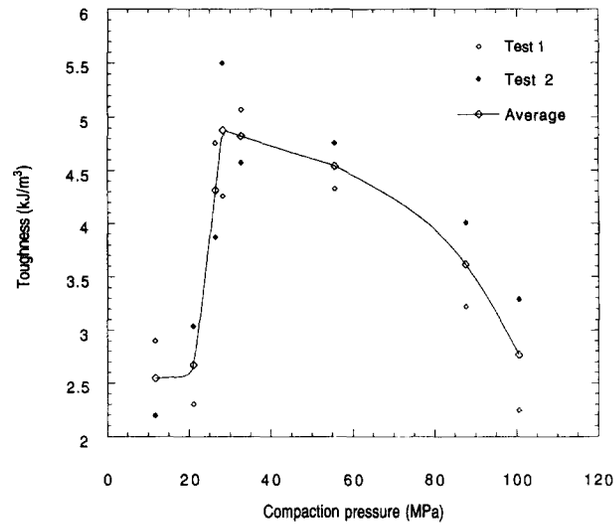

Figure 10 Energy to fracture *versus* compaction pressure measured at the ambient temperature for UHMWPE Hifax 1900 samples compacted at 127°C for 30 min. The ultimate stress–strain, or energy to fracture, reflects the particle interfacial cohesive strength, which is influenced by both particle–particle contact area and free volume. Contact area increases with increasing compaction pressure, but free volume decreases

Thus the degree of chain interfacial diffusion across particle boundaries determines the energy to fracture. As the pressure increases, the particles become closer to each other, and the contact area increases. The increased contact area gives a higher probability for interparticle diffusion giving rise to thicker crystals and higher physical entanglements crossing particle boundaries. The resultant higher interfacial cohesive strength will absorb extra energy before fracture. However, as the free volume decreases and the contact surface area increases with increasing compaction pressure, the product of free volume and contact area may go through a maximum at a certain compaction pressure. When the compaction pressure is raised beyond this critical value, chain movement will start to decline as shown in the solid-state nuclear magnetic resonance (n.m.r.) measurements above the α transition temperature of the material.

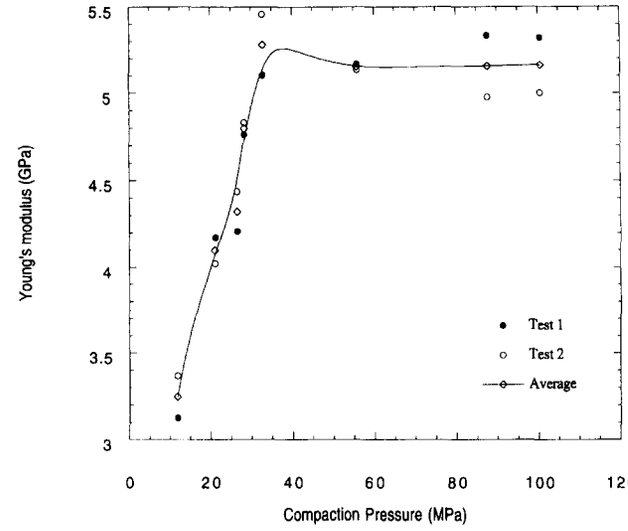

Figure 11 Young's modulus *versus* compaction pressure measured at the ambient temperature for UHMWPE Hifax 1900 samples compacted at 127°C for 30 min. The trend of the data is similar to the bulk density curve; the Young's modulus increases with increasing density or decreasing voidage and reaches a plateau at the maximum density

The Young's moduli of the compacted powders are shown in *Figure 11*. The results appear to follow a similar trend of density with compaction pressure. The Young's modulus increases from 3.1 GPa at a compaction pressure of 11 MPa to a maximum of 5.28 GPa at a compaction pressure of 32 MPa, and then stays nearly constant upon further increase in compaction pressures. This suggests that the rise in modulus is due to the reduction in voids (i.e. increase in bulk density) rather than particle–particle interfacial cohesion which controls the tensile strength. This is confirmed by the fact that the modulus does not fall after the optimum pressure of 30 MPa is reached, whereas T_m, the energy to fracture, and chain mobility data all fall after the optimum compaction pressure is passed. It should also be noted that, under all compaction pressures, the compacted Hifax 1900 powders show a much higher stiffness compared with the melt-crystallized polyethylene materials (approximately 1 GPa). This might be due to the high crystallinity (about 80%) of these compacted powders.

Chain mobility measurement using high-temperature solid-state nuclear magnetic resonance

In order to explain the above observed behaviour and predict the deformability of the compacted materials, chain mobility in the amorphous phase was monitored using solid-state n.m.r. spectroscopy. A standard inversion recovery pulse sequence[15,16] was used to measure the ^{13}C spin-lattice relaxation time, T_1, of the amorphous phase in both the as-received reactor powders and the compacted samples. For the as-received powder samples, the ^{13}C T_1 was measured as a function of temperature for temperatures ranging from ambient to 97°C.

Solid-state n.m.r. experiments were carried out using a JEOL EX-400 n.m.r. spectrometer operating at a ^{13}C resonance frequency of 100.4 MHz in a 9-T external magnetic field. The ^{13}C 90°-pulsewidth was 5.7 μs. The spectrometer is equipped with a variable-temperature, magic angle spinning probe. Samples were placed into 6-mm rotors. Sample spinning rates ranging from 4.0

to 5.5 kHz were easily achieved. Signals were acquired while the proton decoupler was on. 16 scans and 1 dummy scan were used. Adamantane (ADM) was used as an external reference to set a scale of chemical shifts relative to tetramethylsilane (TMS). ADM has two peaks at chemical shift values 29.5 and 38.6 ppm from TMS.

Two peaks at 31 and 33 ppm were resolved in the n.m.r. spectra of our UHMWPE samples. This is in agreement with the literature[16]. The peak at 31 ppm corresponds to the amorphous phase, while the peak at 33 ppm corresponds to the crystalline phase. The crystalline ^{13}C T_1 is of the order hundreds of seconds. By setting a pre-delay of $5T_1$ of the amorphous phase, which is about 10–15 s, we were probing mainly the chain dynamics of the amorphous phase. Therefore, single-exponential relaxation behaviour was observed in our T_1 measurements.

Uncompacted powder samples

Figure 12 shows the spin intensity relaxation behaviour of chains in the amorphous phase of UH210 and Hifax 1900 reactor powder, respectively, measured at 97°C. The value for ^{13}C T_1 is then obtained by least square curve fitting through the data points assuming a single relaxation time using the following equation

$$\frac{I}{I_\infty} = 1 - 2\exp\left(-\frac{\tau}{T_1}\right) \quad (1)$$

where I and I_∞ are the spin intensities at time, τ, and equilibrium, respectively.

The ^{13}C T_1 values obtained in this way for UHMWPE reactor powders are shown in *Figure 13* where the measurements were performed from room temperature to 97°C. At room temperature, little difference was observed for the chain mobility in the amorphous phase for both materials and both show a spin-lattice relaxation time of about 0.5 s. As the temperature increases, the T_1 for both materials increases. However, for Hifax 1900 the T_1 increases more rapidly, especially as the temperature rises above 77°C. For polyethylene, this corresponds to the α transition temperature where the segmental motion of chains become highly rapid[17]. The ^{13}C T_1 data

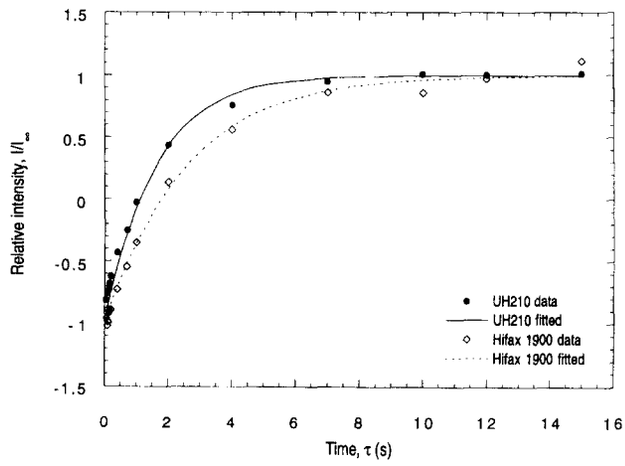

Figure 12 ^{13}C spin intensity relaxation curves for amorphous chains in UHMWPE reactor powders UH210 and Hifax 1900, measured using the inversion recovery technique at 97°C. The chain is more mobile in the amorphous phase of Hifax 1900, and so the relaxation time T_1 is longer

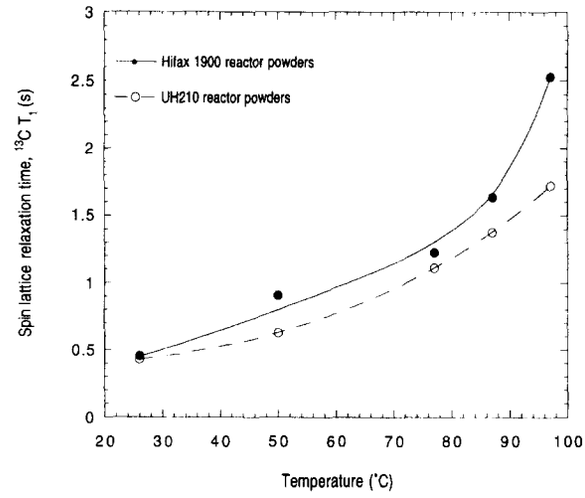

Figure 13 Spin-lattice relaxation time, ^{13}C T_1, as determined from the spin intensity relaxation data for amorphous chains in UHMWPE reactor powders UH210 and Hifax 1900. These two types of powders have the greatest difference in T_1 above the α transition temperature of polyethylene

show the chains in the amorphous region of Hifax 1900 reactor powders are much more mobile than those in the UH210 materials at temperatures above the α transition temperature. It can thus be concluded that the ductility of Hifax 1900 powders is due to the lack of constraints in the amorphous region of the material.

Compacted samples

For compacted UHMWPE rods, the ^{13}C T_1 for chains in the amorphous phase were measured at 97°C. The effect of the compaction pressure on chain mobility as indicated in the ^{13}C T_1 for chains in the amorphous phase is shown in *Figure 14* together with the data for uncompacted Hifax 1900 reactor powder. The result for the compacted samples can again be divided into two regions. The first region ranges from the compaction

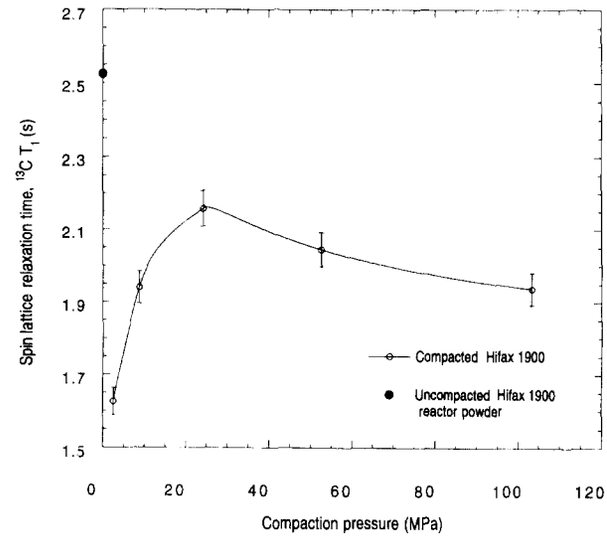

Figure 14 Spin lattice relaxation time ^{13}C T_1 at 97°C for amorphous chains in UHMWPE Hifax 1900 samples compacted at different compaction pressures at 127°C for 30 min. The trend of the data is again indicative that chain mobility, which controls particle interfacial cohesive strength, is influenced by both contact surface area and free volume

pressure of 2.59 to 30 MPa and the second region from 30 to 100 MPa. In the first region, the ^{13}C T_1 increases from 1.6 to 2.2 s, representing an increase in chain mobility. In the second region, the ^{13}C T_1 decreases from 2.2 to 1.9 s, indicating a reduction in chain mobility. The chain mobility results resemble closely to the trend observed for the d.s.c. T_m and mechanical property data, and are consistent with the mechanisms we proposed earlier in terms of the contact surface area and free volume concept.

CONCLUSIONS

The n.m.r. measurement shows that chains in the amorphous region of the Hifax 1900 powders are much more mobile than those of the normal entanglement UH210 reactor powders. The major differences occur at temperatures above the α temperature of the material which is about 70–80°C. The ^{13}C T_1 for the Hifax 1900 powder at 97°C is 2.5 s, which is more than 47% larger than that for the UH210 powder. The high chain mobility observed in the amorphous phase is, therefore, responsible for the high ductility of nascent low entanglement reactor powders[6,7]. This also supports the deformation mechanism for low-entanglement materials proposed by Gerrits and Young[18]. They proposed that the enhancement in drawability in low entanglement powders is mainly due to the *inter-lamellae slip* occurring at low deformation levels. The slip is only possible if a low level of constraints are available within the amorphous phase.

Our experimental findings agree in principle with the particle cohesion mechanism proposed by Gao and Mackley[19] for molten polymer particles. They proposed that the overall time scale for particle interfacial diffusion is controlled by two time variables: contact and diffusion times. The contact time can be fast if the pressure is sufficiently high. The diffusion time is related to the reptation time of the chains in the amorphous phase and is a slow process. In this study, the recrystallization occurs after the chain diffusion so an additional time variable for the recrystallization might also be required. However, at a compaction temperature of 127°C, the recrystallization process for polyethylene is expected to be fast, so it is reasonable to assume the overall time is still controlled by the diffusion time. In the work reported by Gao and Mackley[19], the reptation was considered to be a function of molecular weight only and independent of annealing pressure. Our chain mobility data suggest that a very high compaction pressure slows down chain motion by reducing the free volume available for interfacial diffusion, and thus increases the diffusion time. Modifications to the diffusion time by the addition of free volume parameter are therefore needed to predict the overall interparticle cohesion time.

The mechanical toughness and the high-temperature solid-state n.m.r. measurements suggest an optimum compaction condition exists for the maximum interparticle cohesion and chain mobility. Cohesive samples with high mechanical toughness will ensure that premature failure does not occur during tensile stretching in the process of elongation into high-stiffness and high-strength fibres. The high-chain mobility is necessary for the precursor to exhibit high ductility for further stretching. Our results, therefore, provide optimum compaction conditions such that maximum ductility of the nascent low entanglement reactor powders can be fully realized. The observations here also have direct applications for powder sintering processes, which are the usual processing routes for UHMWPE and PTFE manufacture.

ACKNOWLEDGEMENTS

This work was supported by the Research Grant Council (RGC HKUST580/94E) of Hong Kong. We would also like to thank the Materials Characterisation and Preparation Centre of Hong Kong University of Science and Technology for providing the SEM and n.m.r. facilities.

REFERENCES

1 Smith, P. and Lemstra, P. J. *J. Mater. Sci.* 1980, **19**, 505
2 Mackley, M. R. and Solbai, S. B. *Polymer* 1987, **28**, 1111
3 Gao, P., Mackley, M. R. and Nicholson, T. M. *Polymer* 1990, **31**, 237
4 Gao, P. and Mackley, M. R. *Polymer* 1991, **32**, 3136
5 Mackley, M. R. and Solbai, S. B. *Polymer* 1987, **28**, 1115
6 Kanamoto, T., Ohama, T., Tanaka, K. and Porter, R. S. *Polymer* 1987, **28**, 1517
7 Smith, P., Chanzy, H. D. and Rotzinger, B. P. *Polym. Commun.* 1985, **26**, 258
8 Pawlikowski, G. T., Porter, R. S. and Mitchell, D. J. *J. Polym. Sci., Polym. Phys. Edn* 1988, **26**, 1865
9 Wang, L.-H., and Porter, R. S. *J. Polym. Sci., Polym. Phys. Edn* 1990, **28**, 2441
10 Wunderlich, B. and Cormier, C. M. *J. Polym. Sci., Polym. Phys. Edn* 1967, **5**, 987
11 Tervoort-Engelen, Y. M. T. and Lemestra, P. J. *Polym. Commun.* 1991, **32**, 343
12 Lemestra, P. J. and Kirschbaum, R. *Polymer* 1985, **26**, 1372
13 Leung, T. Y. *MPhil Thesis*, The Hong Kong University of Science and Technology, Hong Kong, 1995
14 Callister Jr., W. D. 'Materials Science and Engineering: an Introduction', 2nd Edn, Wiley, New York, 1991, p. 131
15 Sanders, J. K. M. and Hunter, B. K. 'Modern NMR Spectroscopy: a Guide for Chemists', 2nd Edn, Oxford University Press, Oxford, 1993
16 McBriety, V. J. and Packer, K. J. 'Nuclear Magnetic Resonance in Solid Polymers', Cambridge University Press, Cambridge, 1993
17 Ward, I. M. 'Mechanical Properties of Solid Polymers', John Wiley and Sons, New York, 1971
18 Gerrits, N. S. J. A. and Young, R. J. *J. Mater. Sci.* 1991, **26**, 3137
19 Gao, P. and Mackley, M. R. *Polymer* 1994, **35**, 5210